Journal of Geoscience and Environment Protection, 2026, 14(11), 115-139
https://www.scirp.org/journal/gep
ISSN Online: 2327-4344
ISSN Print: 2327-4336

Geotechnical Characterisation and Rainfall-Sensitive Stability of a Residual Elastic-Silt Slope over Weathered Jurassic Shale at Miritini, Mombasa, Kenya

Charles Ngala Kithome[1], Clifford Arum Obara[2]

[1]Faculty of Engineering and the Built Environment (FEBE), Technical University of Kenya, Nairobi, Kenya
[2]Department of Civil and Resource Engineering (DCRE), Technical University of Kenya, Nairobi, Kenya
Email: charliekithome@gmail.com

How to cite this paper: Kithome, C. N., & Obara, C. A. (2026). Geotechnical Characterisation and Rainfall-Sensitive Stability of a Residual Elastic-Silt Slope over Weathered Jurassic Shale at Miritini, Mombasa, Kenya. *Journal of Geoscience and Environment Protection, 14,* 115-139.
https://doi.org/10.4236/gep.2026.1411006

Received: October 15, 2026
Accepted: November 17, 2026
Published: November 20, 2026

Copyright © 2026 by author(s) and Scientific Research Publishing Inc.
This work is licensed under the Creative Commons Attribution International License (CC BY 4.0).
http://creativecommons.org/licenses/by/4.0/

Open Access

Abstract

Cut and natural slopes on the Jurassic foot plateau west of Mombasa carry pipelines, storage depots and the Standard Gauge Railway, yet the residual soils that mantle them are rarely characterised for stability. This paper presents a geotechnical characterisation of a slope at Miritini, Mombasa County, investigated for a slope-monitoring programme with eight rotary-cored boreholes to 20 m (160 m in total), Standard Penetration Tests, laboratory classification, compaction and shear-box tests, and 32 point-load tests on rock core. The ground comprises 2.5 - 11.5 m of reddish-brown to grey sandy elastic silt (MH; predominantly A-7-5) with local silty sand, over completely to highly weathered, fractured shale that becomes moderately weathered at depth. The silt has liquid limits of 51% - 74%, plasticity indices of 17% - 32% and 29% - 45% clay, with shear-box parameters of c' = 12 - 18 kPa and φ' = 15˚ - 19˚, treated as indicative because the test procedure was not recorded. The shale is a weak rock, with equivalent uniaxial compressive strengths of 5.2 - 8.5 MPa that increase with depth. Groundwater was struck at 0.4 - 11.0 m during water-flush drilling, and ponding was observed near the crest. Hand-held GPS elevations define a 13˚ - 16˚ scarp that falls 37 - 44 m from a 54 - 64 m plateau; an RTK-GNSS survey confirms the analysed gradients (12.6˚ - 15.6˚) and maps ten slope failures, covering 4.9% of the plot, across the scarp, where local faces reach 20˚ - 23˚. Infinite-slope analyses, with the water-table ratio treated as a parametric variable, show that the cohesive cases have FS above unity under the modelled zero-positive-pore-pressure condition (1.5 - 2.1 at 5 m depth) but approach or fall below unity at a representative 11 m soil-rock contact when the water-table ratio exceeds 0.34 - 0.82, depending on slope angle and strength parameters; loss of cohesion and

steeper local gradients can also reduce FS below unity. A saturated mantle would need 32 - 42 kPa of cohesion, over twice the measured value, for FS = 1.3 at that contact. Stability is therefore controlled by pore pressure rather than by soil strength alone. Piezometric and inclinometer monitoring, crest drainage and testing of undisturbed and residual strength are recommended.

Keywords

Slope Stability, Residual Soil, Elastic Silt, Weathered Shale, Infinite Slope, Pore-Water Pressure, Point Load Test, Standard Penetration Test, RTK-GNSS Survey, Miritini, Mombasa

1. Introduction

Rainfall-induced slope failures are a recurring hazard in Kenya, where intense seasonal rainfall acting on deeply weathered soils has caused damaging landslides on hillsides, road cuttings and embankments (Ngecu & Mathu, 1999). Most published Kenyan cases are from the highlands; slopes in the coastal hinterland receive less attention, although the coast receives about 1260 mm of rain a year, much of it concentrated in the April-June long rains (Camberlin & Planchon, 1997). Around Mombasa, the ground rises from the Pleistocene coastal plain onto a Jurassic foot plateau of shales and limestones (Caswell, 1953). The scarp at the plateau edge now carries strategic infrastructure, including oil and gas storage, pipelines and the Standard Gauge Railway (SGR) corridor at Miritini, so the stability of this ground is of practical importance.

Shales and mudstones weather to fine-grained, plastic residual soils whose strength depends strongly on structure, suction and drainage (Wesley, 2010). Their apparent cohesion is often lost when they are wetted, softened or sheared, and their operational strength can decline towards fully softened or residual values (Skempton, 1964; Stark & Eid, 1994). In tropical climates, the controlling mechanism for shallow and intermediate failures in such soils is usually the rise of pore-water pressure during prolonged rainfall rather than a change in the external load (Iverson, 2000; Rahardjo et al., 2007). Assessing such slopes therefore requires the stratigraphy, index properties and strength of the residual soil, the depth to the parent rock, and the groundwater conditions, considered together.

This paper reports a borehole-based geotechnical characterisation of a slope at Miritini, Mombasa County, investigated in May 2026 in support of a slope-monitoring programme. The objectives are to 1) define the stratigraphy and groundwater conditions beneath the slope; 2) characterise the residual elastic silt and the underlying weathered shale using *in-situ* and laboratory tests; 3) evaluate how the factor of safety of the soil mantle varies with slope angle, strength and pore-water pressure using an infinite-slope model; and 4) translate the re-

sults into recommendations for monitoring, drainage and further investigation. The bearing capacities used for the design of associated structures are also summarised and checked.

2. Study Area

2.1. Location and Climate

The site lies within an industrial compound in Miritini Ward, Jomvu Sub-County, next to the Miritini SGR terminus, about 10 km west-north-west of Mombasa Island (**Figure 1**). The reference coordinates are 4˚01'16.0"S, 39˚35'12.2"E. Miritini has grown from a residential area into a transport and logistics hub, and the site is partly vegetated with grass, bush and trees. The climate is hot and humid, with mean daily maximum and minimum temperatures of about 30˚C and 21˚C and a bimodal rainfall regime: the long rains (April-June) deliver most of the annual total of about 1260 mm, and the short rains fall between October and December (Camberlin & Planchon, 1997). No permanent surface water was present during the fieldwork, but localised waterlogging was observed around BH1 at the crest of the slope, indicating poor surface drainage and slow infiltration.

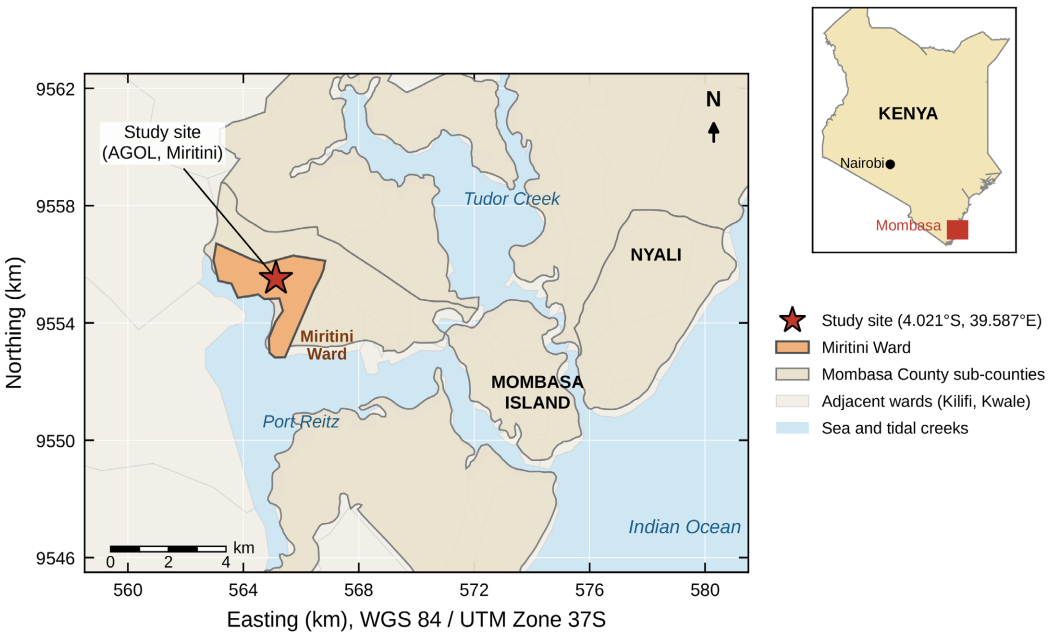


Figure 1. Location of the Miritini study site in Mombasa County, Kenya (WGS 84/UTM Zone 37S; ward and sub-county boundaries from geoBoundaries). The inset shows the position of Mombasa within Kenya.

2.2. Geology and Geomorphology

Gregory (1921) and Caswell (1953) divided the Mombasa hinterland into the Coast Plain of Pleistocene coral reef and sands, the Foot Plateau underlain by Jurassic rocks, and the Nyika and Shimba Hills underlain by the Duruma Sandstones. The Jurassic sequence consists of marine shales and limestones, including the Kibiongoni beds and the Changamwe-Kipevu shales, which dip gently at 5˚ - 10˚ to the

east-south-east and have a planed-off surface that slopes seawards from about 76 m near Mwachi to about 37 m at Changamwe (Caswell, 1953). Miritini lies on this shale outcrop at the margin of the Foot Plateau (**Figure 2**). Where the plateau edge has been dissected by drainage towards Port Reitz and Tudor Creek, it forms scarps on which the shale has weathered in place to a mantle of plastic silt and clay. Unlike the coral-limestone ground of the coastal plain, this mantle is fine-grained and expected to be of low permeability, so it is likely to retain water.

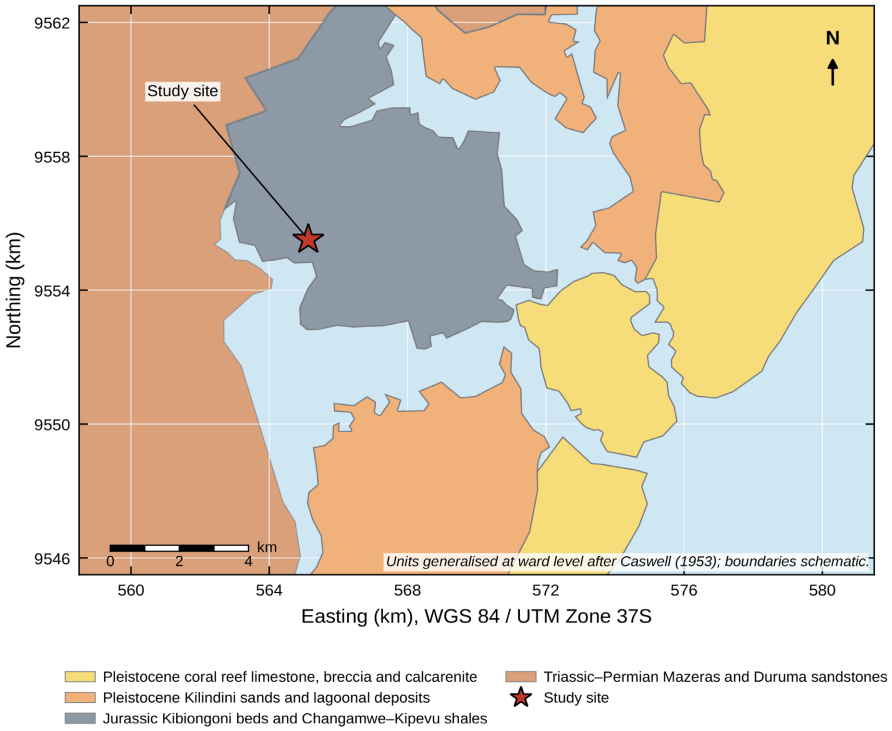


Figure 2. Generalised geology of the Mombasa area showing the position of the study site on the Jurassic shale outcrop (units generalised at ward level after Caswell, 1953).

3. Materials and Methods

3.1. Field Investigation

Eight boreholes (BH1 - BH8) were drilled between 4 and 23 May 2026 at positions selected by the client's engineer to cover the plateau, the scarp and the lower ground (**Figure 3**, **Table 1**). Positions and ground elevations were recorded with a hand-held GPS during drilling and later checked by RTK-GNSS survey (Section 4.8). The vertical accuracy of such units is typically ±3 - 10 m; a value of ±5 m is adopted for each borehole, and its effect on the slope gradients and factors of safety is assessed in Sections 4.1 and 4.7. Drilling used a GY-150 rotary rig with 110 mm casing in soil and an 86 mm double-tube swivel core barrel with water flush in rock, to 20 m in every hole (160 m in total). Fieldwork followed BS 5930:2015 (BSI, 2015). Cores were logged, photographed and boxed (**Figure 4**), and groundwater strikes were recorded during drilling; no standpipes or piezometers were installed, so equilibrium groundwater levels were not measured.

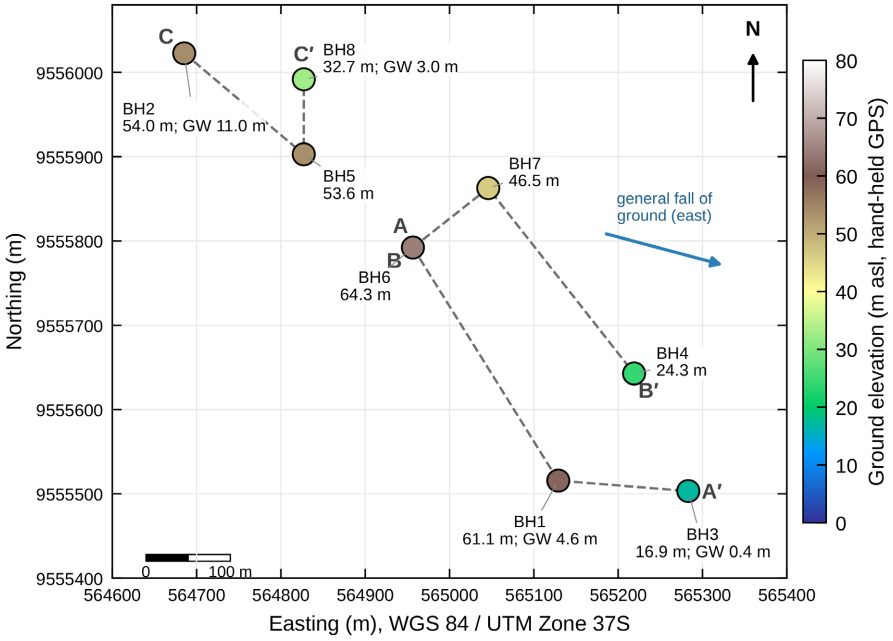


Figure 3. Borehole layout with ground elevations (hand-held GPS), groundwater strikes and the lines of sections A-A', B-B' and C-C'.

Table 1. Borehole locations, elevations, depth to shale and groundwater strikes.

Borehole	Latitude (S)	Longitude (E)	Elevation (m asl)	Depth to Shale (m)	Groundwater Strike (m bgl)
BH1	4˚01'16.0"	39˚35'12.2"	61.1	11.0	4.6
BH2	4˚00'59.5"	39˚34'57.8"	54.0	4.0	11.0
BH3	4˚01'16.4"	39˚35'17.2"	16.9	11.5	0.4
BH4	4˚01'11.9"	39˚35'15.1"	24.3	10.0	Not encountered
BH5	4˚01'03.4"	39˚35'02.4"	53.6	2.5	Not encountered
BH6	4˚01'07.0"	39˚35'06.6"	64.3	9.0	Not encountered
BH7	4˚01'04.7"	39˚35'09.5"	46.5	3.0	Not encountered
BH8	4˚01'00.5"	39˚35'02.4"	32.7	9.0	3.0

Note: all boreholes were drilled to 20.0 m. Depth to shale is the top of completely or highly weathered shale; in BH5, a 5.5 m layer of gravelly elastic silt is interbedded within the shale at 10.0 - 15.5 m. Groundwater strikes were recorded during drilling with water flush and are not equilibrium levels.

Standard Penetration Tests (SPT) were made in the soil overburden with a 63.5 kg automatic trip hammer falling 760 mm, recording the blows for 300 mm of penetration after a 150 mm seating drive, with refusal taken at N = 50. The investigating laboratory reduced N values above 15 with the Terzaghi and Peck dilatancy correction and converted them to allowable bearing pressures. That correction applies only to saturated fine sands and silty sands, and it is not appropriate for the highly plastic elastic silt (MH), so it is not used in this paper. The field N values are used uncorrected and only as an index of consistency for fine-grained

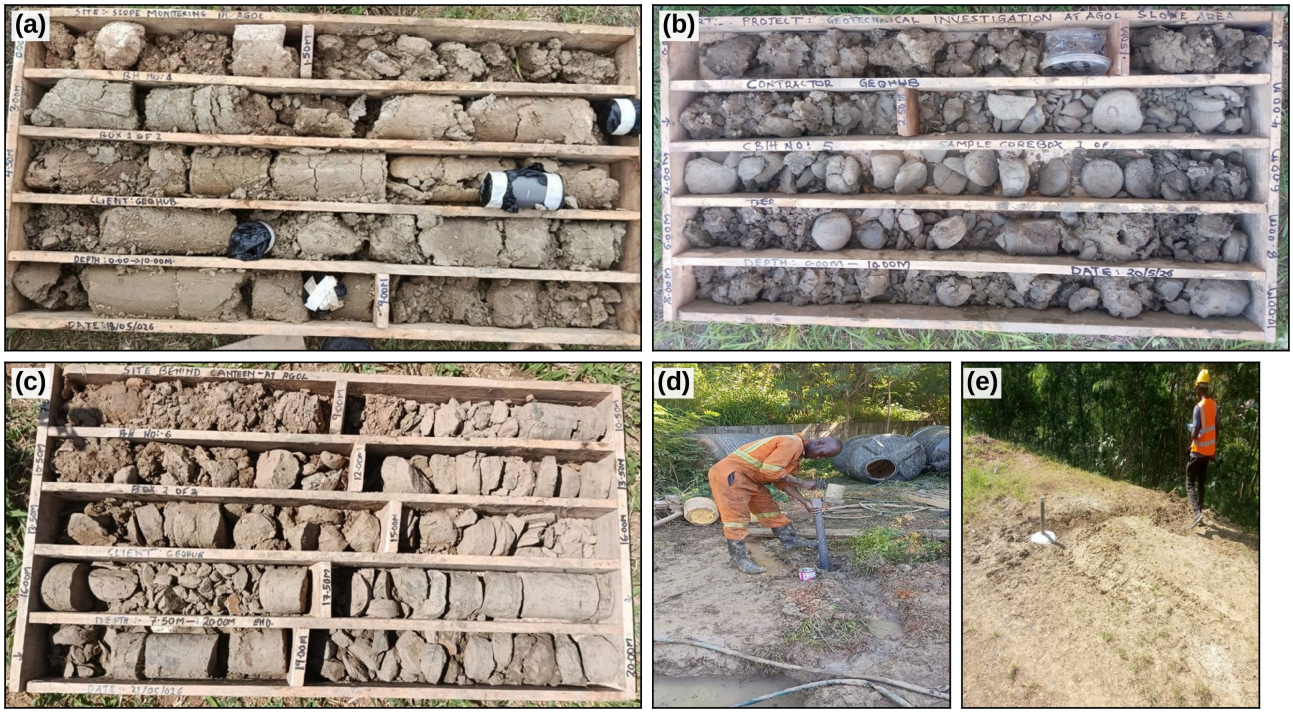


Figure 4. Field and core photographs: (a) core box from BH4, 0 - 10 m, showing the stiff sandy elastic silt; (b) core box from BH5, 0 - 10 m, showing weathered shale recovered as pebbles and cobbles in a silty matrix; (c) core box from BH6, 7.5 - 20 m, showing the transition into highly weathered, fractured shale; (d) drilling on waterlogged ground at the crest; (e) completed borehole on the scarp.

soil (Terzaghi et al., 1996); they are not converted to bearing pressures.

3.2. Laboratory Testing

Bulk samples from the soil horizons (18 samples) and rock cores (32 specimens) were tested in Nairobi by Cransfield Material Testing Centre (CMTC) following BS 1377 (BSI, 1990), ASTM and ISRM procedures (**Table 2**). Soils were classified under the Unified Soil Classification System (ASTM, 2017) and the AASHTO system (ASTM, 2015). The activity A = PI/(clay fraction, %) was calculated from the grading and Atterberg limits (Skempton, 1953). Point-load strength indices

Table 2. Testing programme and standards.

Test	Number	Standard
Standard Penetration Test	52	BS 5930:2015; BS 1377-9
Particle-Size Distribution (Sieve and Hydrometer)	18	BS 1377-2:1990
Atterberg Limits and Linear Shrinkage	18 (15 Plastic)	BS 1377-2:1990
Compaction (Standard Proctor) and Bulk Density	18	BS 1377-4:1990
Direct Shear (Shear Box)	18	BS 1377-7:1990
Point Load Strength Index (Diametral and Axial)	32	ASTM D5731-16; ISRM (1985)

Note: the shear-box test records do not state the consolidation stage or rate of shearing, or whether specimens were undisturbed or reconstituted; the parameters are therefore treated as indicative effective-stress values.

were converted to an equivalent uniaxial compressive strength (UCS) using the conversion factor adopted by the testing laboratory (ISRM, 1985; ASTM, 2016):

$$\mathrm{UCS} = 24\, I_{s(50)} \tag{1}$$

The shear-box results were taken from the laboratory report of the investigation and could not be repeated for this study. The test sheets give the normal stresses, the peak shear stresses and the derived c' and φ', but they do not record whether the specimens were consolidated before shearing, the rate of displacement, or whether the specimens were trimmed from undisturbed soil or reconstituted. Because only bulk samples were taken from the soil horizons, the specimens were probably remoulded, which would destroy the soil structure. The parameters, therefore, cannot be shown to be drained effective-stress values, and they are used here as indicative values only. Three steps are taken to limit reliance on them: lower-bound and cohesionless cases are analysed (Section 3.4), the cohesion needed for given factors of safety is calculated independently of the measured value, and the conclusions are drawn from the trends with pore pressure rather than from absolute values of FS.

3.3. Bearing Capacity

Allowable bearing pressures in soil were computed by CMTC from the shear-box parameters with Terzaghi's bearing-capacity equation for strip footings of width B = 1 - 4 m at embedment depths of 1.5 and 2.0 m, with a factor of safety of 3 (Das, 2007). For rock, the ultimate bearing capacity was estimated from the equivalent UCS with Goodman's (1980) relation for fractured rock, after reducing the UCS by a factor of 5 to allow for fracturing and scale effects, and a design (safe) value was obtained with a factor of safety of 10 (Murthy, 2002):

$$q_u = (\mathrm{UCS}/5)(N_\varphi + 1);\ N_\varphi = \tan^2(45^\circ + \varphi/2);\ q_d = q_u/10 \tag{2}$$

with φ = 20˚ (N_φ = 2.04). The reported values were rechecked against Equation (2) before being summarised; all are preliminary strength-based estimates.

3.4. Slope Stability Analysis

Because the soil mantle is thin compared with the length of the scarp and is underlain by stronger weathered shale, its stability was assessed with the infinite-slope model, which is appropriate for translational slides parallel to the ground surface (Skempton & DeLory, 1957; Duncan et al., 2014). For a slip surface at depth z below a slope of inclination β, with seepage parallel to the slope and a water table at height mz above the slip surface, the factor of safety is:

$$\mathrm{FS} = [c' + (\gamma - m\gamma_w) z \cos^2\beta \tan\varphi']/(\gamma z \sin\beta \cos\beta) \tag{3}$$

where c' and φ' are the effective cohesion intercept and angle of shearing resistance, γ is the bulk unit weight of the soil and γ_w = 9.81 kN/m^3; z is the vertical depth and m = 0 denotes zero positive pore pressure. The analyses adopt γ = 16.3 kN/m^3 (mean bulk density of the silt, 1658 kg/m^3) for dry and saturated cases; illustrative values of 19 - 20 kN/m^3 (not measured) raise FS by 6% - 8% at z = 11 m, β = 15.9˚

and $m = 1$. Three strength cases were considered: the mean shear-box parameters ($c' = 14.7$ kPa, $\varphi' = 16.5^\circ$), the lower-bound parameters ($c' = 12$ kPa, $\varphi' = 15^\circ$), and a cohesionless case ($c' = 0$, $\varphi' = 16.5^\circ$) representing the loss of the cohesion intercept on wetting or softening. Because the shear-box procedure is not documented (Section 3.2) and suction was not measured, the lower-bound and cohesionless cases are treated as the governing cases and the mean case as an upper estimate. Two slope inclinations were analysed, 13.3˚ and 15.9˚, the gradients between BH1 and BH4 and between BH1 and BH3, with $m = 0$, 0.5 and 1.0 and slip depths of up to 11 m, the maximum modelled slip depth. The groundwater strikes are not equilibrium levels, so m is treated as a parametric variable and is not assigned from the strikes. Because the gradients come from hand-held GPS elevations, FS was also calculated over the range of β allowed by the GPS error (Section 4.7). Finally, to test how far the conclusions depend on the measured cohesion, Equation (3) was rearranged to give the cohesion required for a target factor of safety:

$$c'_{\text{req}} = \text{FS}\ \gamma z \sin\beta \cos\beta - (\gamma - m\gamma_w) z \cos^2\beta \tan\varphi' \tag{4}$$

which was evaluated for FS = 1.0 and 1.3 with $\varphi' = 16.5^\circ$.

4. Results

4.1. Stratigraphy and Groundwater

The boreholes show a consistent three-part profile (**Figure 5**). Up to 1.0 m of backfill (gravelly clay and silt) is present at BH1, BH3 and BH4. Beneath it, sandy elastic silt forms the soil mantle; it is reddish-brown in the upper 4.5 - 7.5 m on the plateau (BH1 and BH6) and grey, stiff and locally gravelly below. Lenses of silty sand 2 - 4.5 m thick occur at depth on the lower ground (BH3 at 7 - 11.5 m and BH8 at 7 - 9 m). The base of the silt, which marks the top of the weathered shale, is shallow on the northern part of the plateau (2.5 - 4 m in BH2, BH5 and BH7) and deep beneath the crest and the scarp (9 - 11.5 m in BH1, BH3, BH4, BH6 and BH8). The shale is completely weathered to silty sand in its upper part at BH7 and BH8 and is otherwise highly weathered and highly fractured, being recovered as pebbles and cobbles of shale in a silty matrix (**Figure 4(b)**). Moderately weathered, moderately fractured dark grey shale was reached at 14.7 m in BH2, 19.0 m in BH3 and 13.0 m in BH8.

The borehole elevations define a plateau at 54 - 64 m asl (BH1, BH2, BH5 and BH6) and lower ground at 17 - 33 m asl (BH3, BH4 and BH8). The ground falls 44 m over 155 m between BH1 and BH3 (15.9˚), 37 m over 156 m between BH1 and BH4 (13.3˚), and 21 m over 89 m between BH5 and BH8 (13.2˚). The top of the shale broadly follows the ground surface, so the silt mantle is thickest on the crest and the scarp, where it forms a 9 - 11.5 m layer of plastic soil above the weathered shale. These gradients rest on hand-held GPS elevations. With a vertical error of ±5 m at each borehole, the relief between two boreholes is uncertain by about ±7 m ($\sqrt{(5^2 + 5^2)}$, a root-sum-square estimate for independent errors; the worst case is ±10 m), so the BH1 - BH3 gradient lies between 13.5˚ and 18.3˚

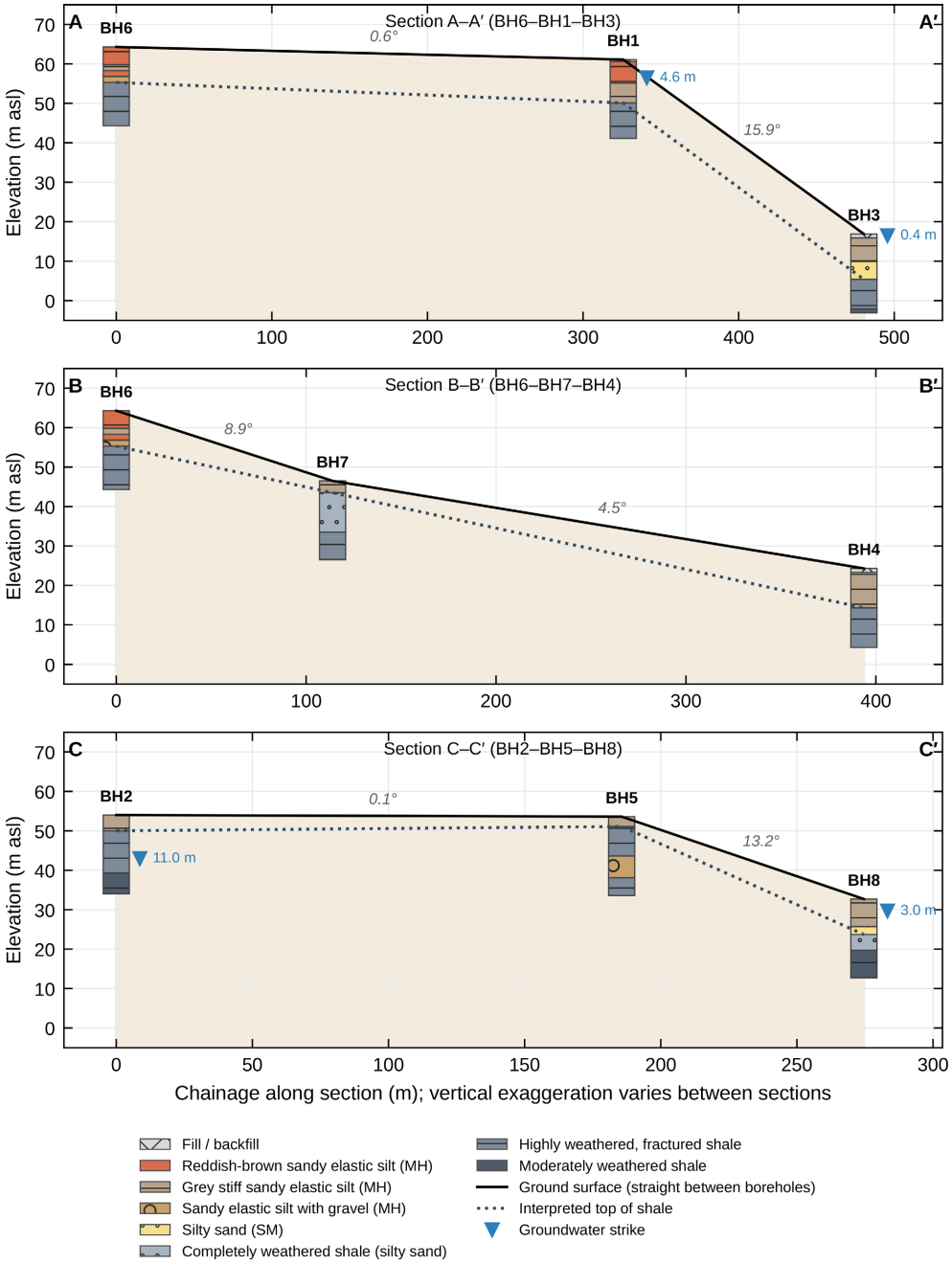


Figure 5. Geological cross-sections A-A', B-B' and C-C' constructed from the borehole logs, showing lithology, interpreted top of shale, groundwater strikes and indicative surface gradients. The ground surface is drawn as straight lines between boreholes.

and the BH1 - BH4 gradient between 10.8˚ and 15.7˚ (Sections 4.7 and 4.8).

Groundwater was struck in four boreholes: at 0.4 m in BH3 at the toe of the scarp, at 3.0 m in BH8 on the lower ground, at 4.6 m in BH1 on the crest, and at 11.0 m in BH2 within the shale. The recorded BH1 strike occurs within the elastic silt at approximately 56.5 m asl, about 39.6 m above ground level at BH3, and together with the ponding seen at the surface, it may indicate a perched or elevated water table held up by the low-permeability silt, a hypothesis that requires piezo-

metric confirmation. These strikes were recorded during drilling with water flush, which adds water to the hole and can mask or raise the level at which groundwater is first seen. No standpipes were installed, and no levels were read after drilling. The strikes therefore show only where water was present at the time of drilling; they are not equilibrium piezometric levels and are not used to fix the water-table ratio in the stability analysis (Section 4.7).

4.2. Penetration Resistance

SPT N values in the elastic silt increase from 9 - 11 at 1 m to 12 - 25 at 4 - 8 m (**Figure 6**). On the consistency scale for fine-grained soils (Terzaghi et al., 1996), the silt is stiff near the surface and very stiff below about 6 m, rather than loose or medium dense as a scale for sands would suggest. Refusal (N = 50) occurred at 4 m in BH2 and BH5, where shale is shallow, and at 10 m in BH4 and BH6, matching the depths to shale in the logs. In BH5, N falls to 29 - 33 at 12 - 14 m in the silt layer within the shale. Uncorrected N values are used throughout, and only as an index of consistency; no bearing pressures are derived from them, because N in a plastic fine-grained soil is only loosely related to its strength and compressibility (Kulhawy & Mayne, 1990).

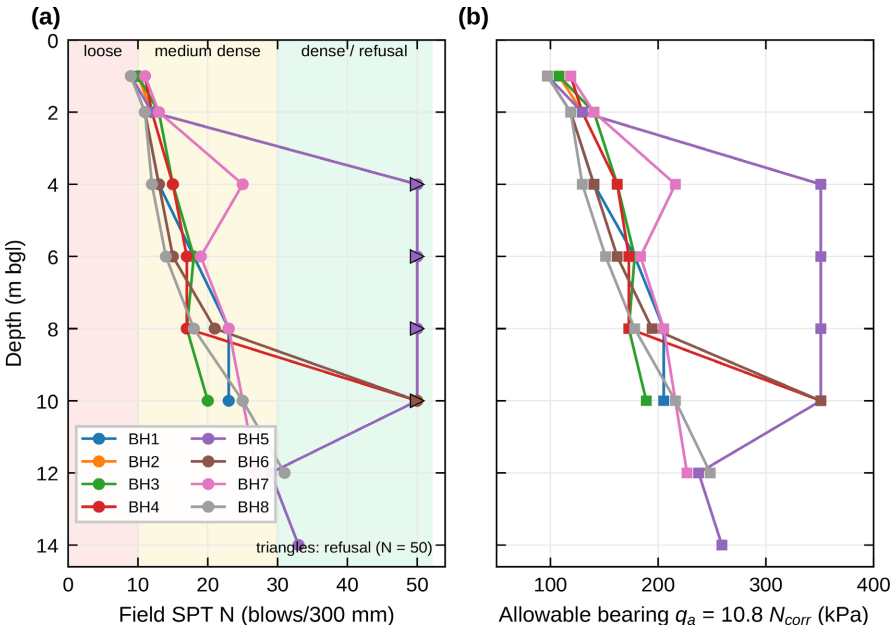


Figure 6. Field SPT N values against depth, with the consistency classes for fine-grained soil of Terzaghi et al. (1996); N values are uncorrected, and triangles mark refusal at N = 50.

4.3. Classification and Compaction

Fifteen of the eighteen soil samples are sandy elastic silt (MH), classified A-7-5 under AASHTO, except for one gravelly sample from BH6 (A-5); the other three are silty sand (SM; A-2-4) (**Table 3**). The elastic silt contains 25% - 48% sand, 18% - 28% silt and 29% - 45% clay, with up to 18% gravel (**Figure 7(b)**). Its liquid limits of 51% - 74% and plasticity indices of 17% - 32% plot below the A-line in

the MH field of the plasticity chart (Figure 7(a)), and its linear shrinkage is 8% - 16%. The activity of 0.53 - 0.84 (mean 0.70) indicates a normally active to inactive clay fraction (Skempton, 1953), which is consistent with clay minerals inherited from weathered marine shale; the mineralogy was not determined. The reddish-brown upper silt in BH1 and BH6 is less plastic (LL 51% - 62%, PI 17% - 24%) and sandier than the grey silt (LL 64% - 74%, PI 26% - 32%), which may reflect a

Table 3. Summary of index, compaction and strength properties.

Property	Elastic Silt (MH), n = 15: Range	MH: Mean	Silty Sand (SM), n = 3: Range
Gravel/sand (%)	0 - 18/25 - 48	5.9/35.8	3 - 12/74 - 82
Silt/clay (%)	18 - 28/29 - 45	22.2/36.2	8 - 14/0 - 5
Liquid limit LL (%)	51 - 74	65.0	Non-plastic
Plastic limit PL (%)	33 - 42	38.5	–
Plasticity index PI (%)	17 - 32	26.5	–
Linear shrinkage (%)	8 - 16	13.1	–
Activity A	0.53 - 0.84	0.70	–
Maximum dry density (kg/m^3)	1230 - 1340	1297	1322 - 1365
Optimum moisture content (%)	20.7 - 32.1	27.8	13.8 - 15.4
Bulk density (kg/m^3)	1494 - 1745	1658	1526 - 1553
Cohesion intercept c' (kPa)	12 - 18	14.7	2 - 3
Angle of shearing resistance φ' (˚)	15 - 19	16.5	23 - 24

Note: classification USCS/AASHTO; MH samples are A-7-5 except one A-5 sample (BH6, 7.5 - 9.0 m).

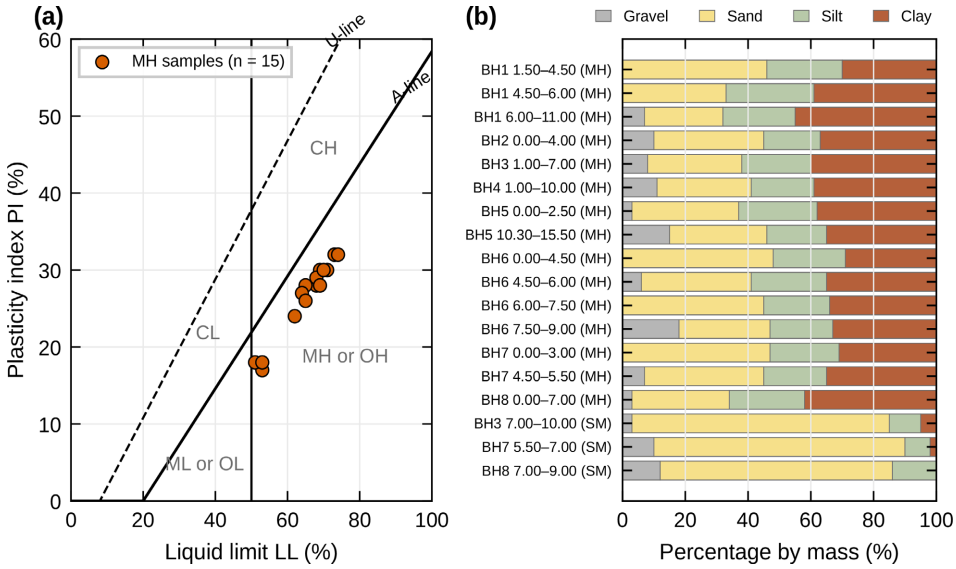


Figure 7. Index properties: (a) Casagrande plasticity chart for the elastic-silt samples; (b) particle-size fractions of all samples (MH = sandy elastic silt; SM = silty sand).

more advanced degree of weathering near the surface.

The standard Proctor maximum dry densities of the silt are low (1230 - 1340 kg/m^3) at high optimum moisture contents (20.7% - 32.1%), and the bulk densities of 1494 - 1745 kg/m^3 are correspondingly low. The A-7-5 and A-5 classes are rated fair to poor as subgrade (ASTM, 2015), so the silt is not suitable for structural backfill or for rebuilding slopes without modification.

4.4. Shear Strength

The shear-box tests on the elastic silt gave c' = 12 - 18 kPa and φ' = 15˚ - 19˚, and those on the silty sand gave c' = 2 - 3 kPa and φ' = 23˚ - 24˚ (**Figure 8(a)**). The angles of shearing resistance of the silt are low for a soil with 25% - 48% sand, and they correlate weakly and positively with plasticity index (r = 0.43), whereas cohesion is uncorrelated with φ' (r = −0.03). The cohesion intercepts are likely to include a contribution from suction and from the structure of the partly dried samples, which will diminish on wetting (Fredlund et al., 2012; Wesley, 2010). No suction measurements, soil-water characteristic tests, or saturated or suction-controlled shear tests were made, so the size of this contribution cannot be quantified. The analyses therefore bound its influence: the cohesionless case and the required cohesion bound the effect of losing part or all of the intercept. For this reason, the cohesionless case in Section 3.4 is treated as a realistic lower bound for long-term conditions rather than as an extreme.

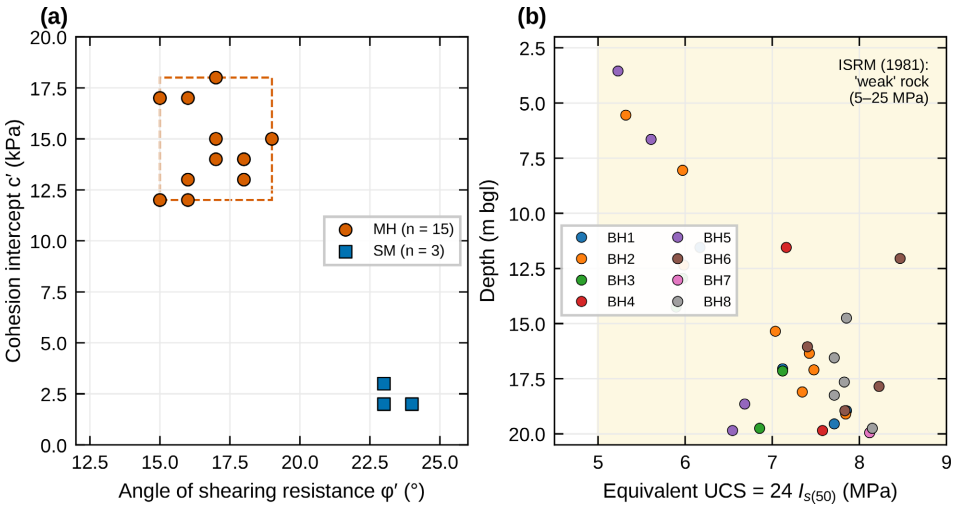


Figure 8. Strength parameters: (a) shear-box cohesion intercept against angle of shearing resistance (the dashed box encloses the MH range); (b) equivalent UCS of the weathered shale from point-load tests against depth.

4.5. Strength of the Weathered Shale

Point-load indices $I_{s(50)}$ of 218 - 353 kPa (mean 296 kPa) give equivalent UCS values of 5.2 - 8.5 MPa (mean 7.1 MPa), which places all specimens in the weak-rock class (5 - 25 MPa) of ISRM (1981) (**Figure 8(b)**, **Table 4**). Strength increases with depth (r = 0.73), from 5.2 - 6.0 MPa in the shallower tested specimens from BH2

and BH5 to 6.5 - 8.2 MPa below 16 m. This matches the progression from highly to moderately weathered shale seen in the cores. The corresponding preliminary safe bearing pressures from Equation (2) are 0.318 - 0.515 MPa.

Table 4. Point-load strength of the weathered shale and derived safe bearing pressure.

Borehole	n	Depth (m)	$I_{s(50)}$ (kPa)	Equivalent UCS (MPa)	Safe Bearing q_d (MPa)
BH1	4	11.6 - 19.6	257 - 327	6.17 - 7.85	0.375 - 0.477
BH2	8	5.6 - 19.1	222 - 327	5.32 - 7.84	0.323 - 0.477
BH3	4	13.0 - 19.8	246 - 297	5.90 - 7.12	0.359 - 0.433
BH4	2	11.6 - 19.9	298 - 316	7.16 - 7.58	0.435 - 0.461
BH5	4	3.6 - 19.9	218 - 278	5.23 - 6.68	0.318 - 0.406
BH6	4	12.1 - 19.0	308 - 353	7.40 - 8.47	0.450 - 0.515
BH7	1	20.0	338	8.12	0.494
BH8	5	14.8 - 19.8	321 - 340	7.71 - 8.15	0.469 - 0.495
All	32	3.6 - 20.0	218 - 353	5.23 - 8.47	0.318 - 0.515

Note: UCS = 24 $I_{s(50)}$; q_d from Equation (2).

4.6. Bearing Capacity of the Soil

The Terzaghi bearing-capacity calculations give safe bearing pressures of 101 - 164 kPa for footings 1 - 4 m wide at 1.5 m depth and 112 - 181 kPa at 2.0 m depth (Table 5). The lowest values are at BH6 and BH1, where the reddish-brown silt has the lowest strength (c' = 12 kPa, φ' = 15˚ - 16˚), and the highest at BH3 and BH4. A check calculation for BH1 (B = 1 m, D_f = 1.5 m) gave an ultimate capacity

Table 5. Safe bearing pressures (kPa) for strip footings from shear-box parameters (FS = 3).

Borehole	D_f = 1.5 m, B = 1 m	D_f = 1.5 m, B = 4 m	D_f = 2.0 m, B = 1 m	D_f = 2.0 m, B = 4 m
BH1	110	120	122	132
BH2	138	153	154	168
BH3	141	159	158	176
BH4	146	164	163	181
BH5	132	142	144	154
BH6	101	110	112	121
BH7	140	153	154	167
BH8	132	142	144	154

Note: computed with Terzaghi's bearing-capacity equation from the shear-box parameters of each borehole (Section 3.3); no bearing pressures are derived from the SPT.

of 333 kPa against the reported 330 kPa. Given the uncertainty in the shear-box parameters (Section 3.2), about 100 kPa is a preliminary estimate for shallow footings in the silt, to be verified for strength, settlement, groundwater, slope-edge effects and foundation geometry; deeper founding on the weathered shale should be evaluated for higher loads, after rock-mass, settlement and slope-interaction checks.

4.7. Infinite-Slope Factor of Safety

The factors of safety for the silt mantle decrease with slip depth and with pore pressure (Figure 9, Table 6). With zero positive pore pressure ($m = 0$), FS exceeds unity for all cohesive cases: at 5 m depth, FS is 1.72 - 2.06 with the mean parameters and 1.50 - 1.79 with the lower-bound parameters, and it remains above 1.15

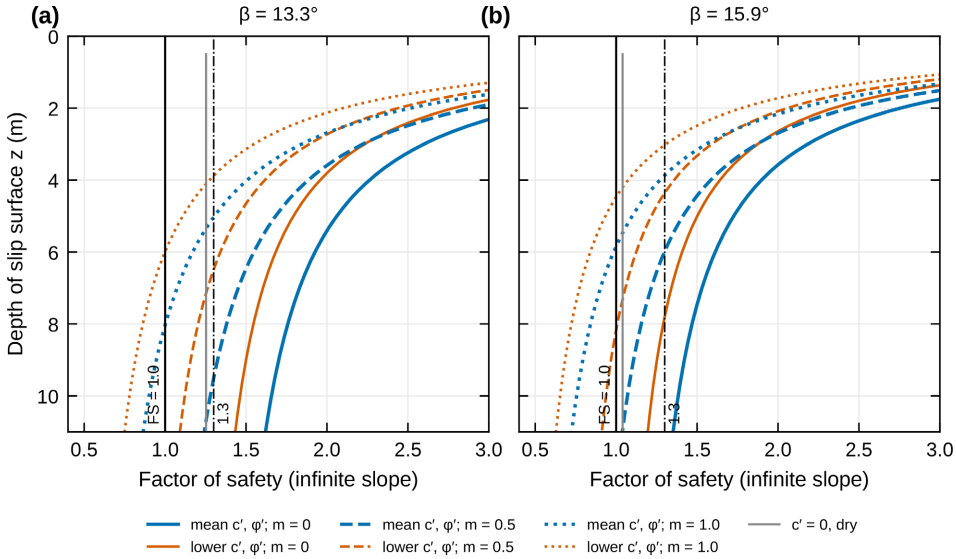


Figure 9. Infinite-slope factor of safety against slip-surface depth for the elastic-silt mantle at slope inclinations of (a) 13.3˚ and (b) 15.9˚, for mean (c' = 14.7 kPa, φ' = 16.5˚) and lower-bound (c' = 12 kPa, φ' = 15˚) parameters, water-table ratios m = 0, 0.5 and 1.0, and the cohesionless dry case.

Table 6. Infinite-slope factors of safety and critical depths of the elastic-silt mantle.

Strength Case	β (˚)	FS at 5 m, m = 0	FS at 5 m, m = 0.5	FS at 5 m, m = 1.0	Depth for FS = 1, m = 1.0 (m)
Mean (c' = 14.7 kPa, φ' = 16.5˚)	13.3	2.06	1.68	1.30	8.0
	15.9	1.72	1.41	1.10	5.8
Lower bound (c' = 12 kPa, φ' = 15˚)	13.3	1.79	1.45	1.11	6.0
	15.9	1.50	1.22	0.93	4.5
Cohesionless (c' = 0, φ' = 16.5˚)	13.3	1.25	0.88	0.50	FS < 1 at all modelled depths
	15.9	1.04	0.73	0.41	FS < 1 at all modelled depths

Note: γ = 16.3 kN/m^3; m = height of the water table above the slip surface divided by its depth.

at the 11 m maximum modelled depth. As the water table rises, the critical depth at which FS = 1 becomes shallower. With a fully saturated mantle (m = 1) and the mean parameters, FS falls to 1.0 at 8.0 m on the 13.3˚ slope and at 5.8 m on the 15.9˚ slope; with the lower-bound parameters, these depths become 6.0 m and 4.5 m. Even with m = 0.5, FS at 10 m is only 1.07 on the 15.9˚ slope with the mean parameters and 0.94 with the lower-bound parameters. Without cohesion, FS equals tanφ'/tanβ at m = 0, which is 1.25 at 13.3˚ and 1.04 at 15.9˚, and it falls to 0.73 - 0.88 at m = 0.5.

The groundwater strikes are not used to assign a value of m, because they were recorded during water-flush drilling and are not equilibrium levels (Section 4.1). Instead, m is treated as a parametric variable, and the value at which a given FS is reached is reported so that it can be compared with piezometer readings when these become available. For a slip at a representative 11 m deep soil-shale contact, FS = 1.0 is reached at m = 0.82 (mean parameters) and 0.63 (lower bound) on the 13.3˚ slope, and at m = 0.56 and 0.34 on the 15.9˚ slope. These correspond to a water table about 2.0 - 4.1 m and 4.8 - 7.3 m below ground, respectively.

Because the slope gradients rest on hand-held GPS elevations, FS was recalculated for the range of gradient allowed by a ±5 m vertical error at each borehole, taken as ±7 m in the relief between two boreholes (root-sum-square; Table 7). This is an illustrative sensitivity range, not a bound. Within it, the FS at 5 m for m = 0 with the mean parameters varies from −15% to +23% of the nominal value. The saturated FS at the 11 m soil-rock contact stays below 1.0 except at the gentlest bound of the BH1 - BH4 gradient (FS = 1.06), and the cohesionless case at m = 0 falls to 0.90 at the steepest bound of the BH1 - BH3 gradient. The absolute values of FS are therefore uncertain by up to about 20%; the cohesive cases remain above unity at m = 0 and the saturated mantle close to or below limiting equilibrium, but loss of cohesion and steeper local gradients can reduce FS below unity; the RTK-GNSS survey described in Section 4.8 confirms the nominal gradients to within 0.7˚.

Table 7. Sensitivity of the factor of safety to slope inclination within the GPS elevation uncertainty.

Gradient	β (˚)	Mean, z = 5 m, m = 0	Mean, z = 5 m, m = 1	Mean, z = 11 m, m = 1	Lower Bound, z = 11 m, m = 1	c' = 0, Dry
BH1 - BH4, −7 m	10.8	2.53	1.60	1.06	0.92	1.55
BH1 - BH4, nominal	13.3	2.06	1.30	0.87	0.75	1.25
BH1 - BH4, +7 m	15.7	1.75	1.11	0.73	0.64	1.05
BH1 - BH3, −7 m	13.5	2.03	1.29	0.85	0.74	1.23
BH1 - BH3, nominal	15.9	1.72	1.10	0.73	0.63	1.04
BH1 - BH3, +7 m	18.3	1.50	0.96	0.63	0.55	0.90

Note: ±7 m is the combined uncertainty in relief for a ±5 m vertical error at each of the two boreholes ($\sqrt{2}$ × 5 m). Mean: c' = 14.7 kPa, φ' = 16.5˚; lower bound: c' = 12 kPa, φ' = 15˚; γ = 16.3 kN/m^3.

To separate the conclusions from the uncertain shear-box cohesion, Table 8 gives the cohesion that would be needed to reach FS = 1.0 and 1.3 with φ' = 16.5˚, calculated from Equation (4). With zero positive pore pressure, no cohesion is needed for FS = 1.0 because tanφ' exceeds tanβ, and FS = 1.3 needs no more than 12.3 kPa. When it is saturated (m = 1), FS = 1.0 needs 9 - 28 kPa and FS = 1.3 needs 15 - 42 kPa; at a representative 11 m deep soil-rock contact, FS = 1.3 needs 32 - 42 kPa, more than twice the measured mean of 14.7 kPa. These values assume φ' = 16.5˚ and the adopted geometry and unit weight; requiring FS = 1.3 is not the same as showing FS below 1.0, and actual stability remains dependent on the strength and pore-pressure assumptions.

Table 8. Effective cohesion intercept (kPa) required for FS = 1.0/FS = 1.3, with φ' = 16.5˚.

β (˚)	Slip Depth z (m)	m = 0	m = 0.5	m = 1.0
13.3	5	<0/0.9	2.3/7.7	9.1/14.6
13.3	11	<0/1.9	5.0/17.0	20.1/32.2
15.9	5	<0/5.6	5.9/12.3	12.6/19.0
15.9	11	<0/12.3	12.9/27.1	27.7/41.9

Note: each pair gives the cohesion required for FS = 1.0/FS = 1.3; values from Equation (4) with γ = 16.3 kN/m^3; "<0" means that friction alone gives FS ≥ 1.0, so zero cohesion is sufficient for that target. Measured c' = 12 - 18 kPa (mean 14.7 kPa).

4.8. RTK-GNSS Topographic Survey and Slope Morphology

To remove the main geometric uncertainty in the analyses, the plot was surveyed by real-time kinematic GNSS (RTK-GNSS) in May 2026 by GeoHub Consultancy Ltd. The survey was tied to a network of eight benchmark control points (GCPs) extending from the plateau to the toe (Table 9), with heights referred to the benchmark datum, and was processed in Civil 3D to a terrain model contoured at 2 m (minor) and 10 m (major) intervals over an aerial orthophoto of the site (Figure 10(a)). RTK-GNSS positions are normally accurate to a few centimetres, far better than the hand-held GPS used during drilling, although elevations interpolated from the contoured terrain model, as used below, are less accurate than the surveyed point heights. Coordinates are on the Arc 1960 datum (Clarke 1880 spheroid) in the UTM Zone 37S grid. The surveyed boundary encloses 12.56 ha (31.04 acres); the area computed here from the plotted boundary agrees to within 0.01%, confirming the geo-referencing of the map sheets. An earlier detailed survey of the slopes at 1:750 mapped the stream channel, two principal gullies on the scarp, boundary walls, culverts and the drain outlets that discharge from the terminal onto the slope.

For the present analysis, the 2 m and 10 m contours, the boundaries of the twelve equal-area elevation classes of the slope morphology map (Figure 10(b)) and the control points were combined into a 2 m grid by linear triangulation and light smoothing, from which ground elevations and slope angles were derived. In

Table 9. RTK-GNSS control points (benchmarks) used for the topographic survey (Arc 1960/UTM Zone 37S; heights to the benchmark datum).

Point	Northing (m)	Easting (m)	Elevation (m)	Nearest Borehole
GCP1	9,556,086.095	564,856.110	61.118	BH6 (6 m)
GCP3	9,556,025.569	564,871.668	61.012	BH6 (67 m)
GCP4	9,556,160.344	564,756.038	50.083	BH5 (49 m)
GCP7	9,556,155.339	564,848.634	48.083	BH6 (65 m)
GCP8	9,556,145.730	564,989.413	40.487	BH7 (44 m)
GCP9	9,556,051.129	565,065.230	34.688	BH4 (124 m)
GCP10	9,555,940.297	565,143.017	19.377	BH4 (22 m)
GCP11	9,555,800.614	565,199.230	13.571	BH3 (13 m)

Note: borehole distances use the hand-held GPS positions of Table 1.

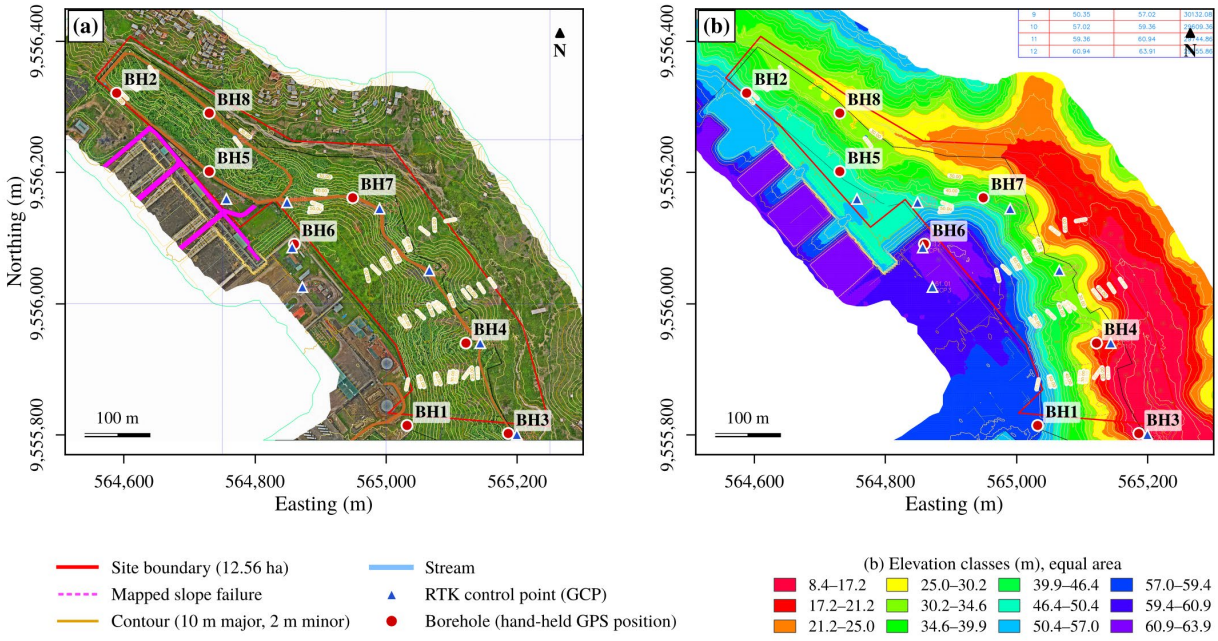


Figure 10. RTK-GNSS survey of the Miritini plot: (a) topographic map on the aerial orthophoto, with 2 m and 10 m contours, mapped slope failures, control points and boreholes; (b) slope morphology map in twelve equal-area elevation classes (8.4 - 63.9 m) covering the full mapped extent of about 36 ha. Grid: Arc 1960/UTM Zone 37S. Survey and drawings by GeoHub Consultancy Ltd (May 2026), re-plotted with borehole positions.

a leave-one-out check, the grid reproduced seven of the eight control heights to within 1.3 m (root-mean-square error 0.5 m). The exception is GCP11 at the toe, which lies below the lowest mapped class boundary (17.2 m), so elevations below about 17 m are taken from the control points rather than from the grid. The surveyed surface ranges from 8.4 m at the stream to 63.9 m on the plateau. The twelve classes have equal areas (2.96 - 3.01 ha each) and together cover about 36 ha, the full extent of the morphology map, which extends beyond the 12.56 ha plot; the area-elevation curve (Figure 11(c)) therefore describes the mapped slope as a

whole, whereas the slope-angle and failure statistics below refer to the plot boundary. The class elevation ranges describe the form of the slope: the plateau above 57 m occupies three classes spanning only 6.9 m, whereas the widest classes (6.5 - 8.8 m) lie on the upper scarp between 39.9 m and 57.0 m and on the lower slope below 17.2 m.

Table 10 compares the hand-held GPS elevations of the boreholes with elevations interpolated from the RTK terrain model at the same positions. The GPS values are higher at every borehole, by 0.7 - 6.7 m (mean 3.6 m, root-mean-square 4.0 m), so the ±5 m allowance of Section 3.1 is exceeded only at BH5. Part of this systematic offset may reflect a difference between the vertical reference of the

Table 10. Hand-held GPS and RTK-GNSS ground elevations at the boreholes.

Borehole	GPS Elevation (m)	RTK Terrain Elevation (m)	GPS − RTK (m)	Local Slope (˚)
BH1	61.1	56.8	+4.3	10
BH2	54.0	49.4	+4.6	17
BH3	16.9	13.6[a]	+3.3	–
BH4	24.3	22.5	+1.8	15
BH5	53.6	46.9	+6.7	6
BH6	64.3	61.0	+3.3	1
BH7	46.5	42.2	+4.3	18
BH8	32.7	32.0	+0.7	11

Note: RTK terrain elevations are interpolated from the terrain model at the positions of Table 1 and are less precise than surveyed point heights; [a]represented by GCP11, 13 m from BH3.

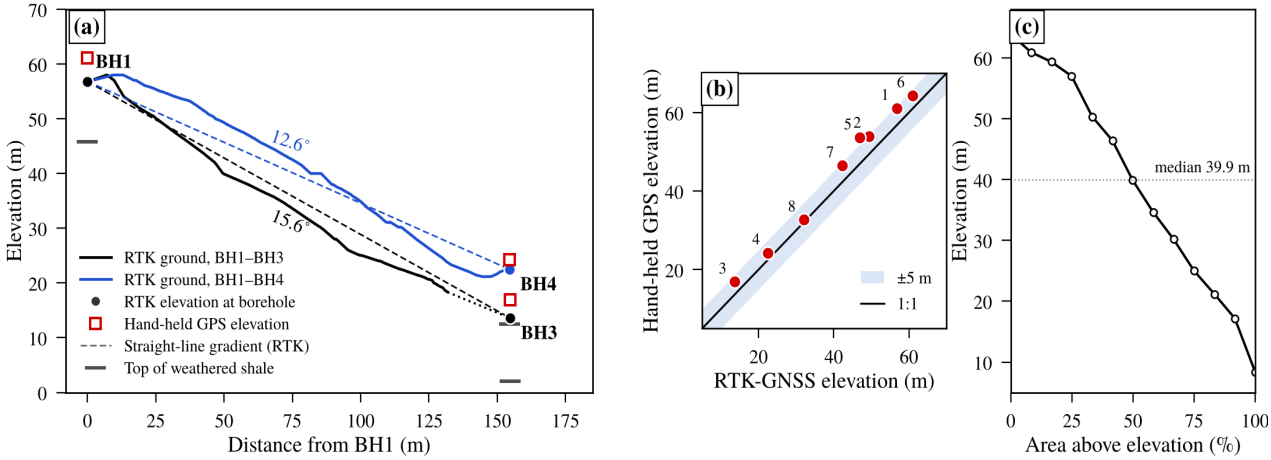


Figure 11. (a) RTK ground profiles along the analysed lines BH1 - BH3 and BH1 - BH4, with the straight-line gradients, hand-held GPS elevations and top of weathered shale; (b) hand-held GPS against RTK-GNSS elevations at the boreholes; (c) area-elevation curve of the full mapped extent (about 36 ha) from the twelve equal-area classes.

hand-held receiver and the benchmark datum of the survey, rather than measurement error alone. Because the offset is largely systematic, the relief between boreholes is better determined than the elevations themselves. The RTK survey gives a fall of 43.2 m over 155 m between BH1 and BH3 (15.6˚) and 34.3 m over 154 m between BH1 and BH4 (12.6˚), against 15.9˚ and 13.3˚ from the GPS (**Figure 11(a)** and **Figure 11(b)**). Both RTK gradients lie within the sensitivity range of **Table 7** and within 0.7˚ of the nominal values used in Section 4.7, so the factors of safety in **Table 6** are representative of the straight-line geometry. The BH5 - BH8 gradient is gentler than estimated (9.5˚ against 13.2˚) because the GPS error is largest at BH5.

The straight lines between boreholes nevertheless average out the steepest parts of the scarp. The slope map derived from the RTK model (**Figure 12(b)**) gives a mean slope angle of 13.7˚ within the plot boundary, with 42% of the area steeper than φ' = 16.5˚, 27% steeper than 20˚ and 7% steeper than 25˚; along the BH1 - BH3 line, the steepest 20 m run is inclined at 23˚. Ten slope failures were mapped in the survey (S1 - S10; **Figure 10(a)** and **Table 11**), and the same areas show visible degradation on the orthophoto (**Figure 12(a)**). They cover 0.62 ha (4.9% of the plot) and lie across the scarp between about 18 m and 58 m elevation. The mean slope angles of the individual failure polygons range from 14.3˚ to 27.3˚, so the failures are not confined to the steepest faces, but their area-weighted mean slope angle is 19.3˚, against 13.7˚ for the plot as a whole, and 73% of their area is steeper than 16.5˚. The largest, S10 (0.20 ha), lies between BH1 and BH4, on the slope represented by the analysed lines.

Table 11. Slope failures mapped in the RTK-GNSS survey, with elevations and slope angles from the RTK terrain model.

Failure	Easting (m)	Northing (m)	Area (m²)	Elevation (m)	Mean Slope (˚)
S1	564,717	9,556,271	350	32.9 - 43.8	17.0
S2	564,977	9,556,171	660	23.8 - 41.5	20.2
S3	565,012	9,556,116	410	26.5 - 39.0	19.9
S4	564,984	9,556,096	230	40.3 - 52.0	27.3
S5	565,034	9,556,082	380	24.3 - 37.7	20.4
S6	565,000	9,556,036	150	53.9 - 58.0	14.7
S7	565,051	9,556,004	690	32.4 - 47.8	18.2
S8	565,104	9,555,967	770	20.7 - 40.3	14.3
S9	565,099	9,555,904	550	22.0 - 39.6	20.9
S10	565,122	9,555,852	2010	17.9 - 38.3	20.4
Total			6200	17.9 - 58.0	19.3

Note: coordinates are outline centroids; areas are from the digitised outlines, rounded to 10 m² (total 4.9% of the plot); total mean slope is area-weighted.

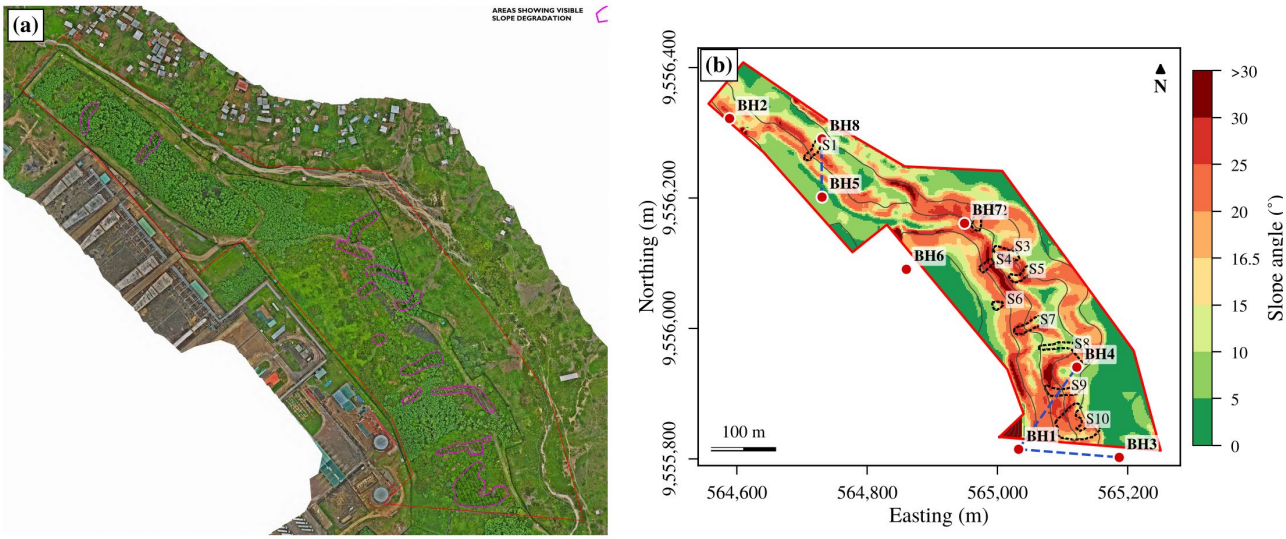


Figure 12. (a) areas of visible slope degradation (magenta, hatched) mapped on the aerial orthophoto; (b) slope angles derived from the RTK terrain model, with the mapped failures S1 - S10, the analysed borehole lines (dashed) and 10 m contours. Classes are divided at φ' = 16.5˚, above which the cohesionless factor of safety is below unity.

Table 12. Infinite-slope factor of safety at the RTK-derived gradients and on steeper local faces (Equation (3), γ = 16.3 kN/m³).

Geometry	β (˚)	Mean, z = 5 m, m = 0	Mean, z = 5 m, m = 1	Mean, z = 11 m, m = 1	Lower Bound, z = 11 m, m = 1	c' = 0, m = 0
BH1 - BH4, RTK	12.6	2.17	1.37	0.91	0.79	1.33
BH1 - BH3, RTK	15.6	1.76	1.12	0.74	0.64	1.06
Local face	20.0	1.38	0.89	0.58	0.50	0.81
Steepest run, BH1 - BH3	23.0	1.20	0.78	0.51	0.44	0.70

Note: mean c' = 14.7 kPa, φ' = 16.5˚; lower bound c' = 12 kPa, φ' = 15˚; steepest run = steepest 20 m of BH1 - BH3.

Table 12 repeats the infinite-slope calculation of Equation (3) for the RTK gradients and for local faces of 20˚ and 23˚. At the RTK gradients, FS differs from the values in Table 6 by no more than 0.11. On the 20˚ - 23˚ faces, the cohesionless case gives FS = 0.70 - 0.81 even with zero positive pore pressure (m = 0), and with the mean parameters and a saturated mantle FS falls to 1.0 at depths of only 3.5 - 4.2 m. The concentration of the mapped failures on faces steeper than φ' therefore supports the conclusion of Section 4.7 that the stability of the mantle depends on pore pressure and on the persistence of the cohesion intercept, and identifies the local faces, rather than the average gradients, as the critical geometry for monitoring and limit-equilibrium sections (Section 5.4).

5. Discussion

5.1. Controls on Stability

The investigation shows that the slope at Miritini is formed of a plastic residual soil, 9 - 11.5 m thick on the crest and scarp, resting on weak, fractured shale whose strength increases with depth. The contrast in strength and permeability at the

base of the silt makes the soil-rock interface the most likely position for a translational slip, as is common in residual soils over weathered mudrocks (Wesley, 2010; Cruden & Varnes, 1996). The analyses show that the margin of safety on this surface depends far more on pore pressure than on the strength parameters within their measured range: going from the mean to the lower-bound parameters reduces FS by 13% - 15%, whereas raising m from 0 to 1 reduces it by 36% - 38% at 5 m depth and by more at greater depths. This is consistent with the dominant role of rainfall infiltration and transient water-table rise in landslides in tropical residual soils (Iverson, 2000; Rahardjo et al., 2007).

Three features of the site make high pore pressures plausible. First, the mantle has a high clay content and low density, so infiltration is expected to be slow, and the soil to drain slowly once wetted, although permeability was not tested. Second, water was struck within the silt at the crest and almost at the surface at the toe, and ponding occurs on the plateau around BH1. Third, the long rains bring a sustained supply of water over two to three months (Camberlin & Planchon, 1997). Moreover, the reddish-brown upper silt is the most weathered and weakest material at the site and is 4.5 - 7.5 m thick beneath the crest (BH1 and BH6), where the scarp begins. The RTK-GNSS survey shows that past movement follows the same pattern: the ten mapped failures lie on scarp faces with a mean inclination of 19.3˚, steeper than $\varphi' = 16.5^{\circ}$, where the cohesionless mantle has FS below unity even with zero positive pore pressure (**Table 11** and **Table 12**).

5.2. Reliability of the Strength Parameters

The φ' values of 15˚ - 19˚ are low for a sandy silt and lie closer to the fully softened and residual strengths of high-plasticity soils than to the peak strengths of intact residual soils (Stark & Eid, 1994; Mitchell & Soga, 2005). This may reflect sample disturbance, fast shearing or genuine softening of the shale-derived silt. Conversely, the cohesion intercepts of 12 - 18 kPa, which contribute much of the computed stability, are unlikely to persist on fully softened or pre-existing shear surfaces (Skempton, 1964). The results for $c' = 0$, which give FS ≈ 1.0 at m = 0 for the 15.9˚ slope, and 0.70 - 0.81 on the 20˚ - 23˚ local faces (**Table 12**), show how much the present margin of safety relies on this intercept. The shear-box procedure was also not recorded (Section 3.2), and the cohesion intercept may include suction that was not measured. **Table 8** quantifies the cohesion required for selected target factors of safety, assuming $\varphi' = 16.5^{\circ}$ and the adopted geometry and unit weight; actual stability remains dependent on the strength and pore-pressure assumptions. These uncertainties also affect the margin of safety at m = 0, which falls to FS = 1.04 - 1.25 if $c' = 0$. Strength testing on undisturbed samples, including suction-controlled direct shear or triaxial tests with measurement of the soil-water characteristic curve to separate suction from true cohesion, consolidated-undrained triaxial tests with pore-pressure measurement and ring shear tests for residual strength, is needed before stabilisation works are designed.

5.3. Interpretation of the Field Data

Two aspects of the field data require care. First, the SPT values are used without the Terzaghi and Peck dilatancy correction that the investigating laboratory applied. That correction was developed for saturated fine sands and silty sands, in which rapid driving induces negative pore pressures and inflates N; it has no basis in a highly plastic silt, much of which lies above the water strikes, where it lowers N arbitrarily. N is therefore used only as an index of consistency (Terzaghi et al., 1996; Kulhawy & Mayne, 1990), and the bearing assessment rests on the shear-box results (Section 4.6). Secondly, the analysed gradients were derived from hand-held GPS elevations and straight lines between boreholes. The RTK-GNSS survey (Section 4.8; **Table 10**) shows that the GPS elevations are 1 - 7 m too high but that the analysed gradients are correct to within 0.7˚. The straight lines do, however, underestimate the local steepness of the scarp, where faces of 20˚ - 23˚ carry the mapped failures; the RTK model should be used to define sections for limit equilibrium analyses with circular and non-circular surfaces.

5.4. Implications for Monitoring and Remediation

The relationship between FS and m (**Figure 9**) gives illustrative screening levels, not operational alarm settings. With the mean parameters on the 15.9˚ slope, a slip at a representative 11 m deep soil-rock contact reaches FS = 1.3 at $m \approx 0.08$ and FS = 1.0 at $m \approx 0.56$ (water table about 4.8 m below ground); with the lower-bound parameters, FS = 1.0 is reached at $m \approx 0.34$ (about 7.3 m below ground), and FS is only about 1.19 even at $m = 0$. On the 20˚ - 23˚ local faces that carry the mapped failures, a saturated mantle reaches FS = 1.0 at only 3.5 - 4.2 m depth with the mean parameters (**Table 12**), so levels derived from the average gradients are not conservative for these faces. Alert levels should be based on pore pressures measured at the slip surface, a validated seepage geometry and a site-specific response plan. The following programme is recommended:

1) Install vibrating-wire piezometers in the silt and at the soil-rock contact at BH1, BH3, BH4 and BH8, read at least weekly and continuously during the long rains, together with a rain gauge on site, to establish equilibrium and storm-response pore pressures (Dunnicliff, 1993).

2) Install inclinometer casings along the BH6-BH1-BH3 line, anchored at least 3 m in competent shale below the potential movement zone (about 22 m at BH3, depth to be confirmed by drilling), with survey prisms on the crest and scarp, and one further casing through the largest mapped failure (S10) between BH1 and BH4.

3) Intercept and remove surface water on the plateau with lined cut-off drains along the crest, prevent ponding near BH1, lead the terminal drain outlets that now discharge onto the slope into lined channels to the stream, and consider sub-horizontal drains into the base of the silt on the scarp to keep m low.

4) Use the RTK-GNSS model (Section 4.8) to set out sections through the mapped failures and the steepest 20˚ - 23˚ faces, repeat the survey after each long-

rains season to detect any movement of the failure scarps; carry out further testing on undisturbed samples (triaxial, ring shear and soil-water characteristic tests, with suction-controlled direct shear or triaxial tests on block or thin-walled tube samples, recording the consolidation stage and rate of shearing) to refine the stability model; and reassess the slope with limit equilibrium and seepage analyses once a full season of piezometric data is available.

5) Avoid placing fill or new loads on the crest and do not reuse the A-7-5 silt as backfill; imported granular fill should be used.

6. Conclusion

This study characterised a slope on the Jurassic shale foot plateau at Miritini, Mombasa, using eight 20 m boreholes, *in-situ* tests, laboratory tests and an RTK-GNSS topographic survey. The main conclusions are:

1) The slope comprises 2.5 - 11.5 m of stiff to very stiff sandy elastic silt (MH; predominantly A-7-5, with one A-5 sample) with local silty sand, over completely to highly weathered, fractured shale that becomes moderately weathered at depth. The silt is thickest (9 - 11.5 m) beneath the crest, the scarp and the lower ground.

2) The silt is highly plastic (LL 51% - 74%, PI 17% - 32%, clay 29% - 45%), of low density, and has shear-box parameters of c' = 12 - 18 kPa and φ' = 15˚ - 19˚, which are treated as indicative because the test procedure was not recorded; the shale is weak rock with an equivalent UCS of 5.2 - 8.5 MPa increasing with depth.

3) Water strikes were recorded at 0.4 - 11.0 m during water-flush drilling, including within the silt at the crest; equilibrium groundwater levels are unknown, and surface ponding indicates poor drainage. The GPS elevations are 1 - 7 m too high, but the RTK-GNSS survey confirms the analysed gradients (12.6˚ - 15.6˚) to within 0.7˚; ten mapped failures covering 4.9% of the plot lie across the scarp, where local faces reach 20˚ - 23˚.

4) The infinite-slope analyses show that the cohesive cases have FS above unity under the modelled zero-positive-pore-pressure condition, but that FS falls to unity at 4.5 - 8 m depth when the mantle is saturated, and at a representative 11 m deep soil-rock contact when m exceeds 0.34 - 0.82, depending on the slope angle and strength parameters. On the 20˚ - 23˚ local faces, the cohesionless mantle has FS = 0.70 - 0.81 even with zero positive pore pressure. Stability is governed mainly by pore-water pressure and by the persistence of the cohesion intercept; loss of cohesion and steeper local gradients can reduce FS below unity (Table 7, Table 8 and Table 12).

5) Preliminary strength-based safe bearing pressures are about 100 - 180 kPa in the silt (the SPT is used only as an index of consistency) and 0.32 - 0.52 MPa on the weathered shale; both require verification.

6) Piezometric and inclinometer monitoring through at least one long-rains season, improved crest drainage, and testing of undisturbed and residual strength are required before any remedial design. The FS-m relationships presented here provide illustrative screening levels for the monitoring programme, and the RTK-

GNSS model allows instruments and analysis sections to be placed on the steepest faces, where the mapped failures are concentrated.

Acknowledgements

The authors thank Africa Gas & Oil Co. Ltd (AGOL) for permission to use the investigation data, GeoHub for the field programme and the RTK-GNSS survey, and Cransfield Material Testing Centre, in particular Elias Morang'a and Eng. Joel Wairua, for the drilling, logging and laboratory testing. FEBE, Technical University of Kenya, is acknowledged for academic support. C. A. Obara contributed to manuscript editing and provided guidance.

Data Availability Statement

The borehole logs, laboratory test sheets and RTK-GNSS survey underlying this study are held by AGOL, Cransfield Material Testing Centre and GeoHub, and are available from the corresponding author on reasonable request with the permission of the data owners. Map boundaries are from geoBoundaries (CC BY 4.0).

Conflicts of Interest

The authors declare no conflicts of interest regarding the publication of this paper.

References

American Society for Testing and Materials (ASTM) (2015). *ASTM D3282-15: Standard Practice for Classification of Soils and Soil-Aggregate Mixtures for Highway Construction Purposes*. ASTM International.

American Society for Testing and Materials (ASTM) (2016). *ASTM D5731-16: Standard Test Method for Determination of the Point Load Strength Index of Rock and Application to Rock Strength Classifications*. ASTM International.

American Society for Testing and Materials (ASTM) (2017). *ASTM D2487-17: Standard Practice for Classification of Soils for Engineering Purposes (Unified Soil Classification System)*. ASTM International.

British Standards Institution (BSI) (1990). *BS 1377:1990: Methods of Test for Soils for Civil Engineering Purposes* (Parts 1-9). BSI.

British Standards Institution (BSI) (2015). *BS 5930:2015: Code of Practice for Ground Investigations*. BSI.

Camberlin, P., & Planchon, O. (1997). Coastal Precipitation Regimes in Kenya. *Geografiska Annaler: Series A, Physical Geography, 79,* 109-119. https://doi.org/10.1111/j.0435-3676.1997.00010.x

Caswell, P. V. (1953). *Geology of the Mombasa-Kwale Area (Report No. 24)*. Geological Survey of Kenya.

Cruden, D. M., & Varnes, D. J. (1996). Landslide Types and Processes. In A. K. Turner, & R. L. Schuster (Eds.), *Landslides: Investigation and Mitigation (Special Report 247)* (pp. 36-75). Transportation Research Board.

Das, B. M. (2007). *Principles of Foundation Engineering* (6th ed.). Thomson.

Duncan, J. M., Wright, S. G., & Brandon, T. L. (2014). *Soil Strength and Slope Stability* (2nd ed.). Wiley.

Dunnicliff, J. (1993). *Geotechnical Instrumentation for Monitoring Field Performance*. Wiley.

Fredlund, D. G., Rahardjo, H., & Fredlund, M. D. (2012). *Unsaturated Soil Mechanics in Engineering Practice*. Wiley. https://doi.org/10.1002/9781118280492

Goodman, R. E. (1980). *Introduction to Rock Mechanics*. Wiley.

Gregory, J. W. (1921). *The Rift Valleys and Geology of East Africa*. Seeley, Service & Co.

International Society for Rock Mechanics (ISRM) (1981). *Rock Characterization, Testing and Monitoring: ISRM Suggested Methods*. Pergamon Press.

International Society for Rock Mechanics (ISRM) (1985). Suggested Method for Determining Point Load Strength. *International Journal of Rock Mechanics and Mining Sciences & Geomechanics Abstracts, 22,* 51-60.

Iverson, R. M. (2000). Landslide Triggering by Rain Infiltration. *Water Resources Research, 36,* 1897-1910. https://doi.org/10.1029/2000wr900090

Kulhawy, F. H., & Mayne, P. W. (1990). *Manual on Estimating Soil Properties for Foundation Design (Report EL-6800)*. Electric Power Research Institute.

Mitchell, J. K., & Soga, K. (2005). *Fundamentals of Soil Behavior* (3rd ed.). Wiley.

Murthy, V. N. S. (2002). *Geotechnical Engineering: Principles and Practices of Soil Mechanics and Foundation Engineering*. Marcel Dekker.

Ngecu, W. M., & Mathu, E. M. (1999). The El-Nino-Triggered Landslides and Their Socioeconomic Impact on Kenya. *Environmental Geology, 38,* 277-284. https://doi.org/10.1007/s002540050425

Rahardjo, H., Ong, T. H., Rezaur, R. B., & Leong, E. C. (2007). Factors Controlling Instability of Homogeneous Soil Slopes under Rainfall. *Journal of Geotechnical and Geoenvironmental Engineering, 133,* 1532-1543. https://doi.org/10.1061/(asce)1090-0241(2007)133:12(1532)

Skempton, A. W. (1953). The Colloidal Activity of Clays. In *Proceedings of the 3rd International Conference on Soil Mechanics and Foundation Engineering* (Vol. 1, pp. 57-61). ICOSOMEF.

Skempton, A. W. (1964). Long-Term Stability of Clay Slopes. *Géotechnique, 14,* 77-102. https://doi.org/10.1680/geot.1964.14.2.77

Skempton, A. W., & DeLory, F. A. (1957). Stability of Natural Slopes in London Clay. In *Proceedings of the 4th International Conference on Soil Mechanics and Foundation Engineering* (Vol. 2, pp. 378-381). Butterworths Scientific Publications.

Stark, T. D., & Eid, H. T. (1994). Drained Residual Strength of Cohesive Soils. *Journal of Geotechnical Engineering, 120,* 856-871. https://doi.org/10.1061/(asce)0733-9410(1994)120:5(856)

Terzaghi, K., Peck, R. B., & Mesri, G. (1996). *Soil Mechanics in Engineering Practice* (3rd ed.). Wiley.

Wesley, L. D. (2010). *Geotechnical Engineering in Residual Soils*. Wiley. https://doi.org/10.1002/9780470943113